• Original Paper •

LASG Global AGCM with a Two-moment Cloud Microphysics Scheme: Energy Balance and Cloud Radiative Forcing Characteristics

Lei WANG[1,3], Qing BAO[*1,2], Wei-Chyung WANG[4], Yimin LIU[1,2,3], Guo-Xiong WU[1,3], Linjiong ZHOU[5], Jiandong LI[1], Hua GONG[1,3], Guokui NIAN[1,3], Jinxiao LI[1,3], Xiaocong WANG[1,2], and Bian HE[1,2]

[1]*State Key Laboratory of Numerical Modeling for Atmospheric Sciences and Geophysical Fluid Dynamics, Institute of Atmospheric Physics, Chinese Academy of Sciences, Beijing 100029, China*

[2]*CAS Center for Excellence in Tibetan Plateau Earth Sciences, Chinese Academy of Sciences, Beijing 100101, China*

[3]*College of Earth and Planetary Sciences, University of the Chinese Academy of Sciences, Beijing 100049, China*

[4]*Atmospheric Sciences Research Center, State University of New York, Albany, New York 12203, USA*

[5]*National Oceanic and Atmospheric Administration, Geophysical Fluid Dynamics Laboratory, Princeton, NJ 08540-6649, USA*

ABSTRACT

Cloud dominates influence factors of atmospheric radiation, while aerosol–cloud interactions are of vital importance in its spatiotemporal distribution. In this study, a two-moment (mass and number) cloud microphysics scheme, which significantly improved the treatment of the coupled processes of aerosols and clouds, was incorporated into version 1.1 of the IAP/ LASG global Finite-volume Atmospheric Model (FAMIL1.1). For illustrative purposes, the characteristics of the energy balance and cloud radiative forcing (CRF) in an AMIP-type simulation with prescribed aerosols were compared with those in observational/reanalysis data. Even within the constraints of the prescribed aerosol mass, the model simulated global mean energy balance at the top of the atmosphere (TOA) and at the Earth's surface, as well as their seasonal variation, are in good agreement with the observational data. The maximum deviation terms lie in the surface downwelling longwave radiation and surface latent heat flux, which are 3.5 W m^{-2} (1%) and 3 W m^{-2} (3.5%), individually. The spatial correlations of the annual TOA net radiation flux and the net CRF between simulation and observation were around 0.97 and 0.90, respectively. A major weakness is that FAMIL1.1 predicts more liquid water content and less ice water content over most oceans. Detailed comparisons are presented for a number of regions, with a focus on the Asian monsoon region (AMR). The results indicate that FAMIL1.1 well reproduces the summer–winter contrast for both the geographical distribution of the longwave CRF and shortwave CRF over the AMR. Finally, the model bias and possible solutions, as well as further works to develop FAMIL1.1 are discussed.

Key words: two-moment cloud microphysics scheme, aerosol–cloud interactions, energy balance, cloud radiative forcing, Asian monsoon region

Article Highlights:

• A physical-based two-moment microphysical scheme is introduced to AGCM FAMIL1.1.
• The model simulates reasonably both the global and regional energy budgets and cloud radiative forcing.
• The model bias as well as the possible solution are also discussed in FAMIL1.1.

---

1. Introduction

The formation and evolution of the Earth's climate system is regulated by spatiotemporal variations in the global energy balance. Clouds play a significant role in the Earth's weather and climate change owing to their influences on the transfer of radiative energy, as well as on the spatial distribution of latent heating in the atmosphere. Indeed, a lack of observational data on clouds and related processes has long been among the major sources of uncertainties in understanding climate change (Bony et al., 2006; Zelinka et al., 2017). Atmospheric aerosols further complicate estimations and interpretations of the changing energy balance in the Earth

* Corresponding author: Qing BAO
  Email: baoqing@mail.iap.ac.cn

system, both through their direct effects (transfer of radiative energy) and indirect effects (aerosol–cloud interactions). Aerosol–cloud–climate interactions are of vital importance in climate system models because of the role they play in global and regional energy balances and cloud radiative forcing (CRF). Climate models is the most commonly used tools for studies on aerosol–climate and aerosol–cloud–radiation interactions (Rosenfeld et al., 2014; Fan et al., 2016). And a comprehensive physically–based cloud microphysics scheme is essential to characterize the part played by aerosols in the nature of clouds and the Earth's climate when investigating aerosol–climate and aerosol–cloud–radiation interactions.

Currently, two types of cloud microphysics schemes are used in climate models: bin microphysics schemes (Feingold et al., 1994; Jiang et al., 2001) and bulk water microphysics schemes (Lin et al., 1983; Reisner et al., 1998; Hong et al., 2002). Bin microphysics schemes divide the particle size spectrum into different bins and can directly simulate the evolution of individual hydrometeors and aerosol particles. In contrast, bulk water microphysics schemes mainly consider the overall spectral distribution of particle sizes, and are therefore suitable for describing the general characteristics of natural cloud precipitation particles (Duan and Mao, 2008). Bin schemes are not suitable for long-term experiments (Roh et al., 2017) because they require large amounts of computation time and memory, especially in global-scale high-resolution experiments. Therefore, bulk water microphysics schemes are commonly adopted in climate models with large domains. Bulk water microphysics schemes can be further subdivided into single-moment and multi-moment schemes on the basis of the number of prognostic variables. The most widely used multi-moment microphysics schemes in climate models are two-moment schemes (Morrison et al., 2005; Seifert and Beheng, 2006; Lim and Hong, 2010). Two-moment microphysics schemes allow greater flexibility in the particle size distribution than single-moment schemes and have been implemented in many state-of-the-art regional and global climate models, such as the WRF model, the CAM5 (Morrison et al., 2005) and the NOAA/GFDL's Atmospheric General Circulation Model (Salzmann et al., 2010). Previous work has also shown that two-moment microphysics schemes provide a better representation of the cloud radiative properties than single-moment schemes, leading to a more accurate simulation of the effects of radiative cooling and heating on circulation patterns (Lee and Donner, 2011).

The IAP/LASG has a long history of working on climate model development (Wu et al., 1996; Bao et al., 2010; Li et al., 2013, 2014b; Zhou et al., 2015), and the latest version of its climate system model is called the FGOALS3. The atmospheric component of FGOALS3 is version 1 of the Finite-volume Atmospheric Model of the IAP/LASG (FAMIL1), which began its development in 2011. With a flexible horizontal resolution of up to 6.25 km, FAMIL1 has been comprehensively evaluated on China's Tianhe-1 and Tianhe-2 supercomputer, and exhibited an excellent performance in term of the computing speed and efficiency (Zhou et al., 2012; Li et al., 2017b). Zhou et al. (2015) evaluated the energy bal-

ance in FAMIL1 and showed that the model performs well in simulations of the annual mean geographical distributions and seasonal cycle of radiative fluxes at the TOA, as well as the latent and sensible heat fluxes at the Earth's surface. However, regional deviations still exist in the model. One of the significant simulation bias in the energy balance modeled by FAMIL1 can be seen in the eastern oceanic regions. Also, in East Asia—a very important climatic region with large anthropogenic–aerosol loading because of its high levels of industrial and domestic emissions, the aerosol–cloud–climate interactions require further verification. However, FAMIL1 uses a bulk water microphysics scheme with a single moment (Lin et al., 1983; Harris and Lin, 2014) and therefore cannot physically describe the aerosol–cloud interactions at the process level at that time. Therefore, in this study, FAMIL1 was coupled with a physically based two-moment, six-class bulk water cloud microphysics scheme (CLR2) (Chen and Liu, 2004; Cheng et al., 2007, 2010) with the aim to better describe the aerosol–cloud interactions and relevant microphysical processes in a new iteration of the model, FAMIL1.1.

Using a standardized Atmospheric Model Intercomparison Project (AMIP) experiment with a horizontal resolution of 2°, the global and regional [focusing on the Asian monsoon region (AMR)] characteristics of the simulated energy balance and CRF in FAMIL1.1 were evaluated. Specific aims of the study included: (1) to assess the model's performance in reproducing the global energy balance with CLR2; (2) to identify the main biases in the simulated energy balance and the possible reasons for them; and (3) to evaluate the model's performance in reproducing the CRF and cloud macro-physical features over the AMR.

The remainder of this paper is organized as follows. Section 2 describes FAMIL1.1, CLR2, and the experimental design. Section 3 describes the observational and reanalysis data used in the evaluation. Section 4 reports the energy balance and relevant cloud–radiation properties modeled by FAMIL1.1. Finally, a summary of the key findings and some further discussion comprises section 5.

2. Model description and experimental design

2.1. *Model description*

The horizontal resolution of FAMIL1.1 is Cube-sphere 48 (C48, about 200 km) and the vertical resolution is a 32-layer hybrid vertical grid with a model top of 2.16 hPa (the vertical height is about 40 km). Most of the physical parameterization schemes in FAMIL1.1 are the same as those used in FAMIL1 (Zhou et al., 2015), the major update in FAMIL 1.1 is the incorporation of the CLR2, which considers the coupling processes in aerosol–cloud–radiation–climate interactions. In addition, the planetary boundary layer (PBL) scheme was updated, from a non-local scheme (Holtslag and Boville, 1993) to a higher order turbulence closure scheme from the University of Washington (Bretherton and Park, 2009) to obtain a realistic value for the turbulence kinetic energy (TKE), which is required to couple the CLR2.

The CLR2 simulates cloud–aerosol interactions through the activation of cloud droplets from cloud condensation nuclei (CCN) and the restoration of aerosols from the evaporation of cloud droplets. Details of all the microphysical processes in the CLR2 were reported by Cheng et al. (2010). Collaborative research and further development on this scheme were reported by Wang et al. (2017). This scheme has previously been coupled to regional climate models to investigate the impacts of aerosols on the cloud microphysics, radiative properties of clouds, precipitation, and tropical cyclones, et al. (Cheng et al., 2010; Hazra et al., 2013; Chen et al., 2015, 2018; Yang et al., 2018). However, the microphysics scheme used in regional climate models cannot be applied directly in global climate models because of "grid-resolution problems" (Wood et al., 2002). For instance, the number of cloud droplets activated at the cloud base shows a strong sensitivity to the saturation excess; and saturation excess is highly dependent upon updraft velocity. However, the grid-box mean updraft velocity is often too low and can be easily averaged out in a GCM with coarse resolution. A sub-grid treatment should be therefore used in GCM to mitigate this problem. In FAMIL1.1, the sub-grid-scale updraft velocity [(Eq. 1)] is used to calculate the activation of aerosol particles based on the general theory of isotropy (Pinto, 1998):

$$w' = \sqrt{\frac{2}{3}\text{TKE}}\,, \qquad (1)$$

where w' is the vertical motion and TKE is the turbulence kinetic energy.

The CFMIP Observation Simulator Package (COSP) has also been coupled online with FAMIL1.1 to provide simulated clouds against the satellite products. COSP is an integrated satellite simulator and enables the conversion of simulation information from model data into several satellite-borne active and passive sensor products, which facilitates the use of satellite data to evaluate a model's simulation performance in a consistent way. This simulator established a bridge between both model–satellite and model–model intercomparisons (Bodas-Salcedo et al., 2011).

2.2. *Experimental design*

A standardized AMIP experiment (prescribed SST) was used to evaluate the energy balance and CRF. The easy-designed AMIP-type experiments are regarded as standard testbeds for the evaluation of the physics schemes and enables to focus on the atmospheric model without the added complexity of ocean-atmosphere feedbacks in the climate system. The advantage of an AMIP experiment is that it does not require a long spin-up to achieve model stability. Also, the so-called climate-drift problem in air–sea coupled models can be avoided. However, the absence of air–sea coupling process will affect the simulation for atmospheric circulation over monsoon regions, thus impact the large-scale background for cloud production. Although another air–sea coupled experiment integrated for a long time was available, AMIP experiment was still used to test the performance of the

microphysics scheme in this study. The model (FAMIL1.1), with a monthly output, was integrated from 1979 to 2009 and the last nine years (2001–09) simulations were extracted for comparison with the observational and reanalysis data. The average background in the CLR2 (Whitby, 1978) is chosen to describe the aerosol number density distribution. The mass loading of the prescribed aerosol in FAMIL1.1 was taken from NCAR Community Atmosphere Model with Chemistry (CAM-Chem) (Lamarque et al., 2012), which were the aerosol data recommended for CMIP5. Based on previous reports (Abdul-Razzak and Ghan, 2000), external mixing processes were considered in the activation processes of the CCN activity of sulfate aerosols and sea-salt aerosols.

3.   Datasets

The following data were used to evaluate the simulated energy balance: (1) monthly radiative flux data from the Clouds and Earth's Radiant Energy System–Energy Balanced and Filled (CERES-EBAF) edition 2.8 dataset; (2) monthly surface sensible and latent heat flux data from the European Centre for Medium-Range Weather Forecasts (ECMWF) Reanalysis Interim (ERA-Interim) dataset; and (3) monthly cloud water data from the CloudSat 2B-CWC-RO version R04 data product. The horizontal resolutions of the CERES-EBAF and ERA-Interim datasets are $2° \times 2°$ and $1° \times 1°$, respectively; both cover the period 2001–09. The CloudSat dataset is remapped from the satellite pixels to the $2.5° \times 2.5°$ longitude–latitude box, which is the resolution commonly used in previous studies (Sassen and Wang, 2008; Ellis et al., 2009). The CloudSat datasets covered the period 2007–11.

4.   Results

4.1.   *Annual global mean energy balance of the Earth*

The Earth's annual global mean energy balance at the TOA and on the surface obtained from FAMIL1.1 are firstly compared to that from several different datasets, including satellite products, reanalysis data, and the outputs from the CMIP5 models (Fig. 1). Those datasets parallel that of Zhou et al. (2015). The simulated global annual mean radiation fluxes at the TOA and at the Earth's surface, as well as the heat fluxes at the Earth's surface, are in good agreement with the observations. For example, the maximum deviation terms lie in the surface downwelling longwave radiation (SDLR) and surface latent heat flux (SLHF), which are 3.5 W m^{-2} (1%) and 3 W m^{-2} (3.5%), respectively. All the energy fluxes from FAMIL1.1 are within the uncertainty ranges of either Stephens et al. (2012) or Wild et al. (2013), or both, and within the maximum/minimum range of the 22 CMIP5 models. The other radiation flux terms, under all-sky (Table 1 and Fig. A1 in the Appendix) and clear-sky conditions (Table 2 and Fig. A1), also show that FAMIL1.1 is in good agreement with CERES-EBAF, albeit with some biases. This means that the model reproduces the global annual mean of the energy
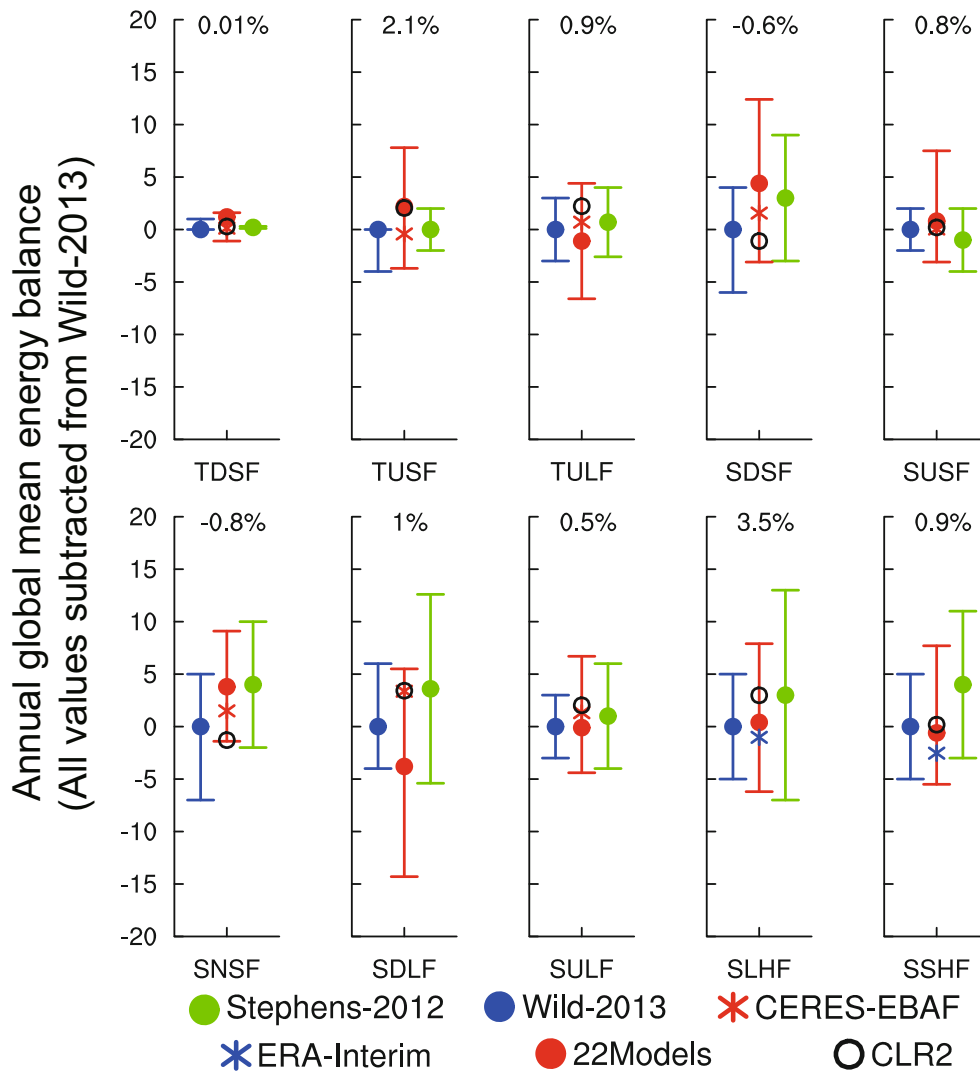
Fig. 1. Annual global mean energy balance at the top of the atmosphere (TOA) and at the Earth's surface in different datasets, including satellite products, reanalysis data, and the outputs from the 22 CMIP5 models. Units: W m^{-2}. Those datasets parallel that of Zhou et al. (2015). The results have been subtracted from the values estimated in Wild et al. (2013). Green, blue and red error bars show the uncertainty ranges of two observational datasets, and the maximum and minimum values of the 22 CMIP5 models, respectively. The relative deviations [compared with Wild et al. (2013)] are listed at the top of echo subplot. The meaning of the abbreviations are as follows. TUSR—TOA upwelling shortwave radiation; TULR—TOA upwelling longwave radiation; SDSR—surface downwelling shortwave radiation; SUSR—surface upwelling shortwave radiation; SNSR—surface net shortwave radiation; SDLR—surface downwelling longwave radiation; SULR—surface upwelling longwave radiation; SLHF—surface latent heat flux; SSHF—surface sensible heat flux.

balance reasonably well.

4.2. *Seasonal cycle of the global mean energy balance*

To evaluate in more depth the performance of FAMIL1.1 in simulating the energy balance, the seasonal cycle of the global mean energy balance was compared with CERES-EBAF and ERA-Interim data (Fig. 2). The CERES-EBAF satellite products were used to compare the radiative fluxes at the TOA and at the Earth's surface, whereas the ERA-Interim reanalysis data was used to compare the surface latent heat fluxes and surface sensible heat fluxes (SSHF) at the

Earth's surface. The results show that the simulated seasonal cycle and amplitude of the radiation fluxes, as well as the surface heat fluxes, agree well with those from the observational/reanalysis data. For example, the TOA upwelling longwave radiation (TULR), the surface downwelling shortwave radiation (SDSR), and the surface upwelling longwave radiation (SULR), show strong seasonal cycles. They are generally stronger during the summer and weaker during the winter and have amplitudes of about 10, 10, and 5 W m^{-2}, respectively. FAMIL1.1 shows an equivalent change to these fluxes. The seasonal variations in the SLHF and the SSHF have weaker
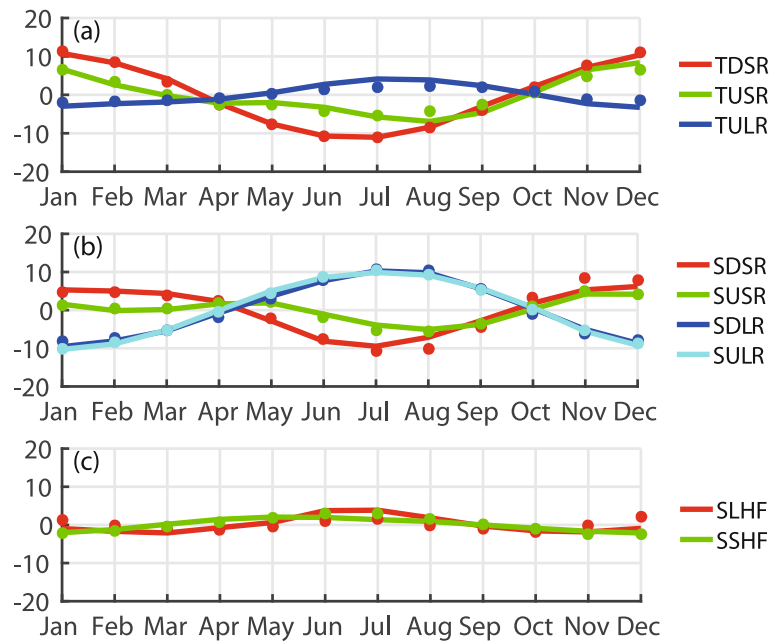
Fig. 2. Seasonal cycle of global mean (a) TOA radiation fluxes, (b) surface radiation fluxes from CERESF-EBA (circles), and (c) surface sensible heat and latent heat fluxes calculated from ERA-Interim (circles) and FAMIL1.1 (lines). The results have been subtracted from their global annual mean values. Units: W m^{-2}. Abbreviations as in Fig. 1.

Table 1. Comparisons for all-sky conditions. Hereafter, the * means positive downward.

Terms	Obs.	FAMIL1.1	FAMIL1.1 minus Obs.
TOA Upwelling Shortwave Radiation	99.58	102.05	2.47 (2.48%)
TOA Upwelling Longwave Radiation	239.7	238.24	−1.46 (−0.61%)
Surface Downwelling Shortwave Radiation*	186.56	183.9	−2.66 (−1.43%)
Surface Upwelling Shortwave Radiation	24.06	24.19	0.13 (0.54%)
Surface Upwelling Longwave Radiation	398.32	399.02	0.7 (0.18%)
Surface Downwelling Longwave Radiation*	345.37	345.42	0.05 (0.01%)
Surface Net Shortwave Radiation*	162.5	159.7	−2.8 (−1.72%)
Surface Net Longwave Radiation*	−52.95	−53.6	−0.65 (1.23%)
Surface Net Total Flux*	109.55	106.1	−3.45 (−3.15%)

Table 2. Comparisons for clear-sky conditions.

Terms	Obs.	FAMIL1.1	FAMIL1.1 minus Obs.
TOA Upwelling Shortwave Radiation	52.48	52.36	−0.12 (−0.23%)
TOA Upwelling Longwave Radiation	265.84	260.25	−5.59 (−2.10%)
TOA Net Shortwave Radiation*	287.64	287.92	0.28 (0.10%)
Surface Downwelling Shortwave Radiation*	244.06	243.67	−0.39 (−0.16%)
Surface Upwelling Shortwave Radiation	29.66	29.91	0.25 (0.84%)
Surface Upwelling Longwave Radiation	398.31	399.02	0.71 (0.18%)
Surface Downwelling Longwave Radiation*	316.43	323.07	6.64 (2.10%)
Surface Net Shortwave Radiation*	214.4	213.77	−0.63 (−0.29%)
Surface Net Longwave Radiation*	−81.88	−75.95	5.93 (−7.24%)
Surface Net Total Flux*	132.51	137.82	5.31 (4.01%)

amplitudes (< 3 W m^{-2}) than the other variables in both the reanalysis datasets and the FAMIL1.1's simulation. Thus, FAMIL1.1 simulates both the seasonal cycle and amplitude of the energy balance reasonably well.

4.3. *Geographical distribution of the annual mean global energy balance*

Global mean energy fluxes are of vital importance in characterizing the total energy balance in the atmosphere.

However, global means may mask underlying regional differences in energy balance. Thus, the geophysical distributions of various radiation fluxes are shown to further investigate the performance of FAMIL1.1 in simulating the global energy balance and regional biases. The most important term in the energy balance is the TOA net radiative flux, which represents the total effect of all the terms connected to the energy balance. The net radiative flux at the TOA is affected by

the TOA downwelling shortwave radiation (TDSR), the TOA upwelling shortwave radiation (TUSR), and the TULR. The TUSR synthetically characterizes the total solar shortwave radiation reflected by the earth system, including the comprehensive reflection effects of clouds, surface/ocean albedo, and aerosols; et al. In contrast, the TULR represents the total outgoing longwave radiation emitted by the earth system, which is determined by the structure of atmospheric temperature, the concentration of greenhouse gases, the temperature/height of clouds, and the land/water emissivity, et al.

Figure 3 shows the annual mean geographical distribution of the TOA net radiation fluxes, the TUSR, and the TULR from the FAMIL1.1 and CERES-EBAF. Compared with CERES-EBAF, FAMIL1.1 reasonably reproduces the spatial distribution of the net radiative fluxes, as well as the TUSR and the TULR, with high spatial correlations of around 0.97, 0.98, and 0.99, respectively. However, the RMSE is relatively large, at around 16.78, 16.83, and 9.75 W m^{-2} for the net radiative flux, the TUSR and the TULR, respectively. Figure 3c shows that the main regional bias arises because the net radiative flux over the most mainland areas in FAMIL1.1 is less than that observed (positive downward), with large negative deviations in northern Africa and northern South America. The maximum negative deviation is about

60 W m^{-2}. The net radiative flux over the Southern Ocean in FAMIL1.1 is also less than that observed (deviation of about -20 W m^{-2}). By contrast, the tropical eastern Pacific Ocean is an area of positive deviations (maximum deviation of about 50 W m^{-2}). These biases are mainly aroused from the simulated biases in the geographical distribution of the TULR and TUSR. In northern Africa and northern South America, both the reflected shortwave radiative flux (maximum deviation of about 50 W m^{-2} or 16%) and the upwelling longwave radiative flux (maximum deviation of nearly 10 W m^{-2} or 5%) are stronger than observed, which means that more of the radiative flux is reflected upward into space and contributes to the negative deviation in the net radiative flux. The deviations in the Southern Ocean are mainly due to a stronger reflected shortwave radiative flux (deviation of about 20 W m^{-2} or 18%). Over the tropical eastern Pacific Ocean, where persistent marine stratocumulus clouds are present, the reflected shortwave cloud radiation is weaker than observed (maximum negative deviation of about 40 W m^{-2} or 50%), whereas the outgoing longwave radiative flux agrees well with the observations, contributing to the overall positive deviation. Comparing Fig. 3f and 3i also shows that deviation in the net radiation flux derives mainly from the simulated bias of the reflected shortwave radiation over most of the regions,
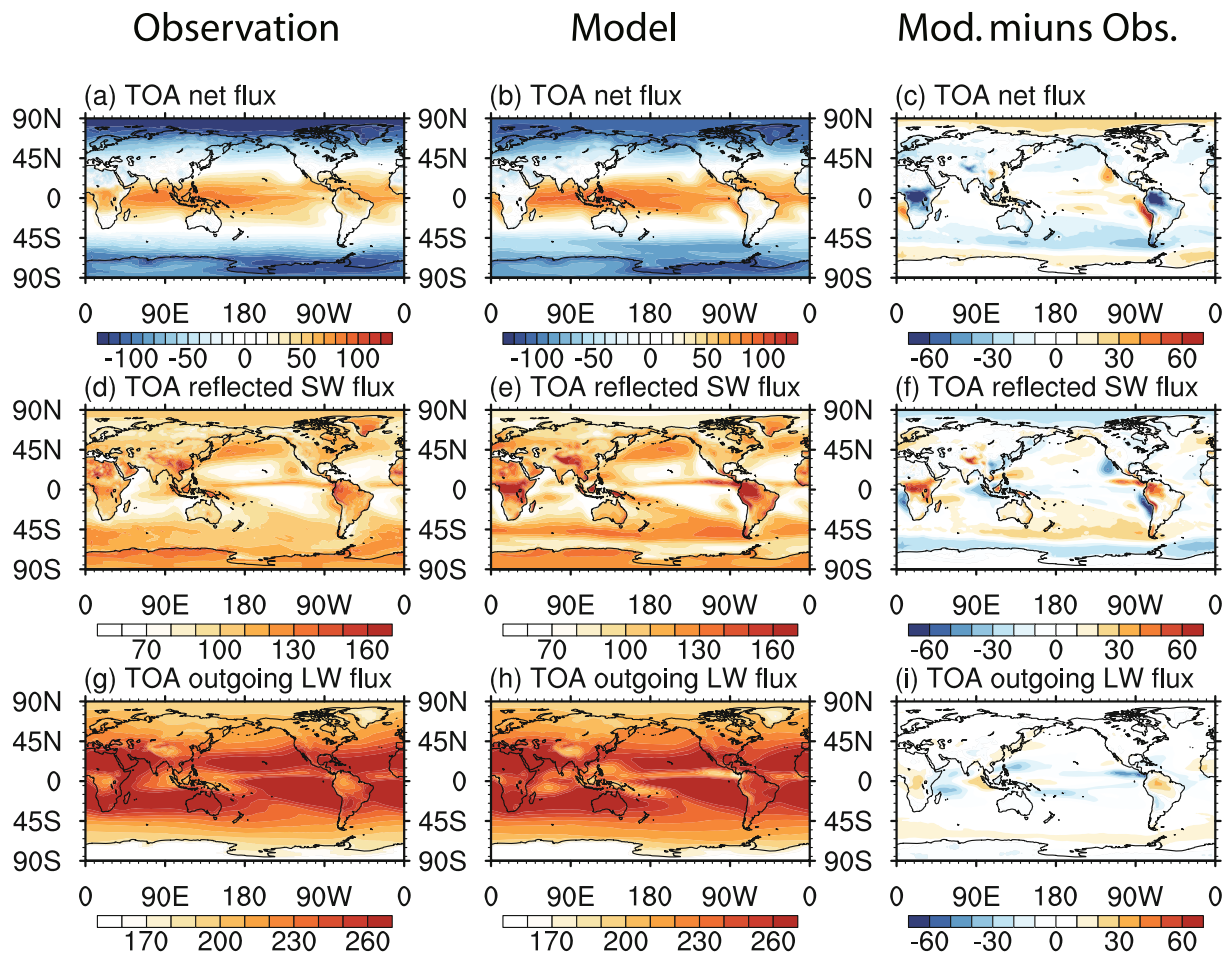

Fig. 3. Geographic distribution of the TOA radiation flux from FAMIL1.1 and observation (CERES-EBAF): (a–c) net radiation fluxes; (d–f) reflected shortwave radiation fluxes; (g–i) outgoing longwave radiation fluxes. Units: W m^{-2}.

such as the Southern Ocean, northern Africa, northern South America, and the tropical eastern Pacific Ocean, in addition to the Atlantic Ocean. The reflected shortwave radiation biases here should both result from the simulation bias for clouds and the ocean/land albedo, in addition to the aerosol's direct effect.

Because the CLR2 mainly affects the progress of cloud microphysics and therefore contributes to the CRF and energy balance of the Earth system, the ability of the model to simulate the CRF was further explored. Figure 4 shows the annual mean geographical distribution of the CRF in the atmosphere from the FAMIL1.1 and observations. FAMIL1.1 reproduces the spatial distribution of both the shortwave and longwave CRF reasonably well (spatial correlations of 0.96 and 0.93, respectively). However, the RMSEs for the shortwave and longwave CRF are 16.53 and 10.76 W m^{-2}, respectively. Figure 4f shows that the model produces a weaker longwave CRF almost everywhere, meaning there is a greater outgoing longwave radiative flux, as shown in Fig. 3i. The shortwave radiative forcing is stronger in the model than observed in northern Africa, northern South America, and the Southern Ocean, but weaker in the tropical eastern Pacific Ocean, the tropical eastern Indian Ocean, and the tropic eastern Atlantic Ocean. And the maximum deviation in these areas is almost 50 W m^{-2}. These deviations are important contributors to the biases in the TOA reflected shortwave radiative fluxes.

Theoretically, the simulated bias in the cloud water content may have a good relationship with the deviation in the simulated shortwave cloud radiation, whereas the simulated bias in the amount of high clouds contributes to the simulated bias in the simulated longwave radiation forcing (Gettelman and Sherwood, 2016). Figure 5 shows the cloud water path (CWP) and amount of high clouds from the COSP simulator and from observation (satellite retrievals). FAMIL1.1 reproduces the basic spatial distribution of the CWP in the CloudSat retrievals (Fig. 5a and 5b), but with some regional biases. FAMIL1.1 tends to simulate a higher CWP over the oceans (including the tropical eastern Pacific Ocean, the Indian Ocean, and the Atlantic Ocean, except for the eastern oceans), and there is almost twice the amount of cloud water over the land (e.g., South America and northern Africa) in the FAMIL1.1 than that in the satellite retrieval data. Figures 4 and 5 show that there is a good agreement for the simulation biases between the shortwave CRF and CWP. The shortwave CRF is stronger than the observed over the Southern Ocean, the northern Pacific Ocean, South America, and northern Africa, where the CWP is overestimated. By contrast, the CWP is underestimated over the eastern oceans, with a weaker shortwave CRF in FAMIL1.1. The model also reproduces a similar spatial distribution of the high clouds amount to the observational data, with a spatial correlation of around 0.94 (Fig. 5d and 5e). However, the high clouds amount is underestimated over South America, northern Africa, the Southern Ocean, and the northern Pacific Ocean, relative to the observations, with a maximum negative bias of 20%. The simulated bias for high clouds amount shows a good relationship with the simulated bias for the longwave CRF. For example, the amount of high cloud is underestimated over South America and northern Africa, with a weaker longwave CRF over these regions.

4.4. *East Asian energy balance and effects of aerosols*

The AMR is an important climatic region with high observed concentrations of aerosols loading (Wang et al., 2012; Zhang et al., 2012). The distribution of the aerosol opti-
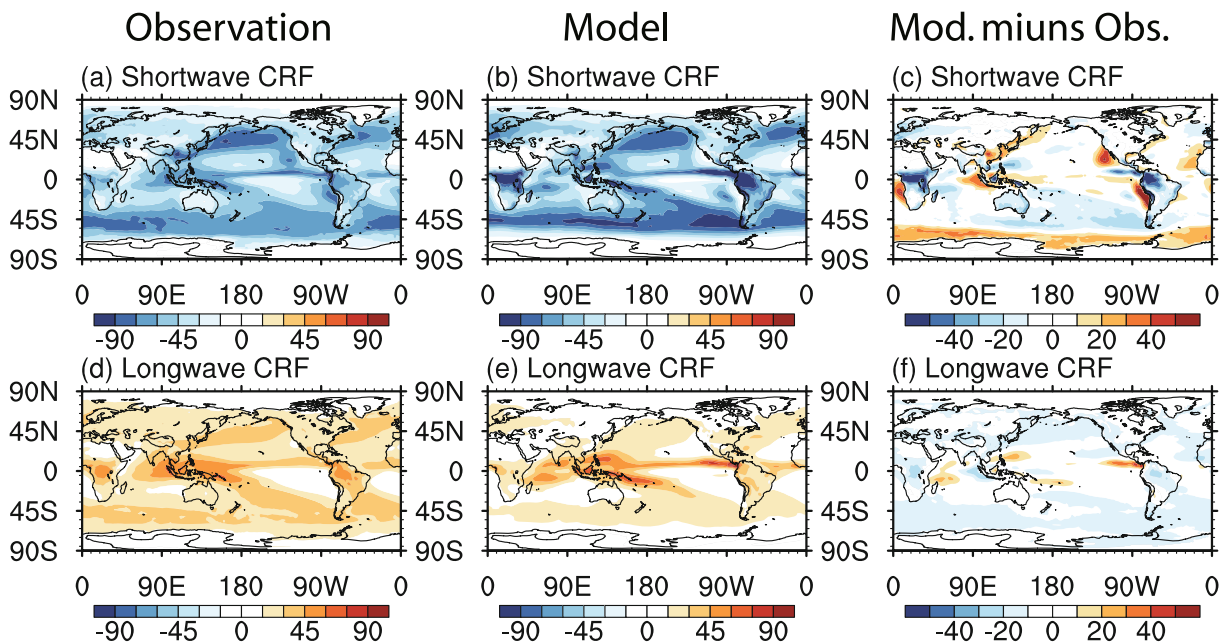

Fig. 4. Geographic distribution of cloud radiation forcing from FAMIL1.1 and observation (CERES-EBAF): (a–c) shortwave cloud radiation forcing; (d–f) longwave cloud radiation forcing. Units: W m^{-2}.
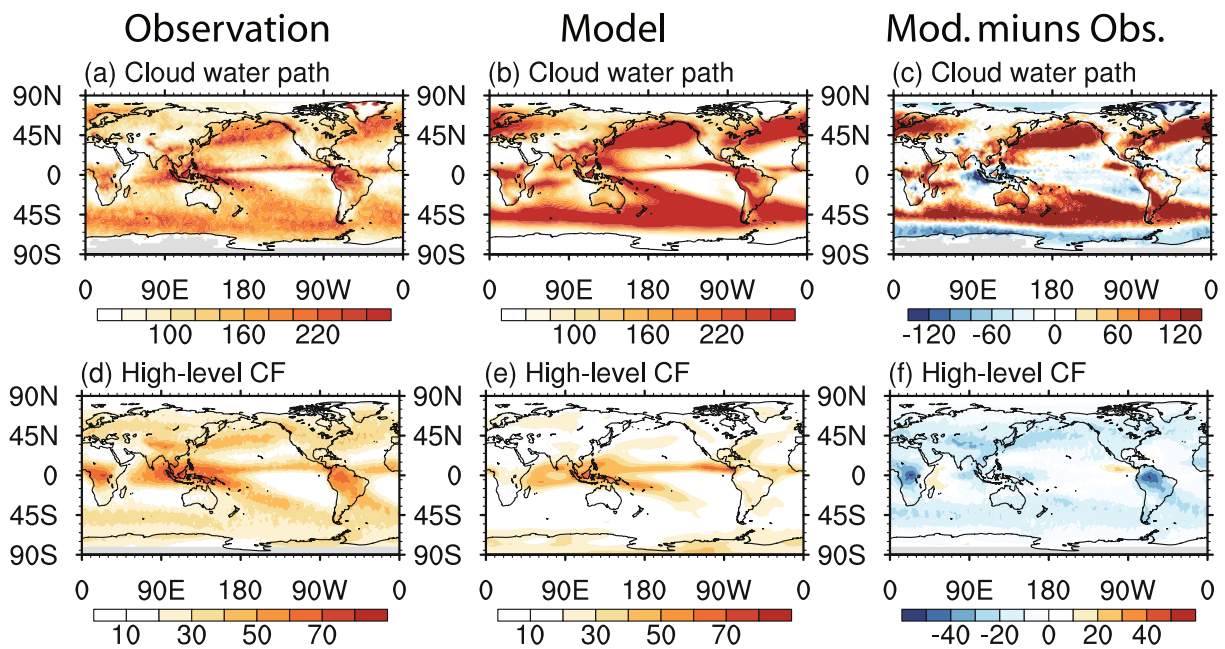
Observation | Model | Mod. miuns Obs.

Fig. 5. Geographic distribution of the cloud water path and amount of high level clouds from observation (CloudSat/CALIPSO) and FAMIL1.1 (with the COSP simulator): (a–c) cloud water path (units: mg m^{-2}); (d–f) high level clouds fraction (CF) (units: %).
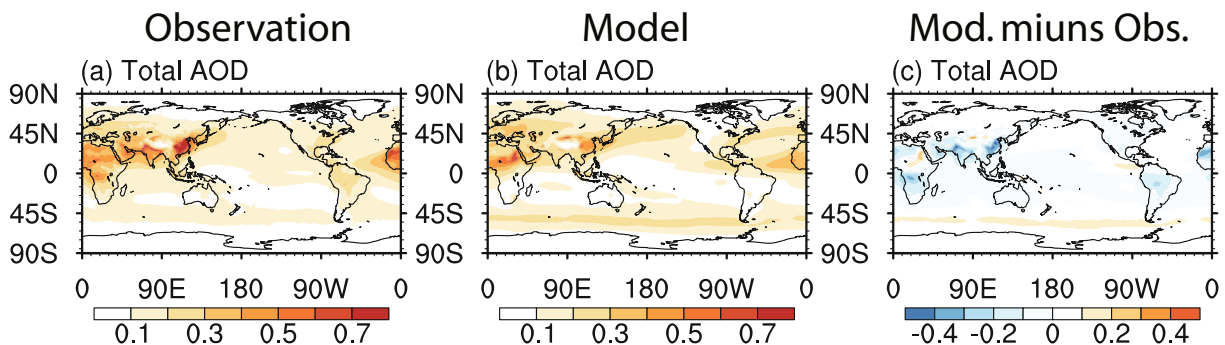

Fig. 6. Geographical distribution of total aerosol optical depth (AOD) at 0.55 μm from (a) observation (MODIS) and (b) FAMIL1.1.

cal depth (AOD) at 0.55 μm is a good representation of the distribution of the total aerosol loading. Figure 6 shows the geographical distribution of the total AOD at 0.55 μm from the observation (MODIS) and FAMIL1.1. The model reproduces the distribution of AOD well, although it underestimates the AOD over East Asia (about 0.5 in FAMIL1.1, but > 0.7 in the observational dataset). The underestimated AOD over East Asian mainly may result from that the aerosol mass concentrations over East Asian are underestimated to some extent (Li et al., 2014a), which is also one of the important causes for the TOA radiation fluxes bias. Figure 7 shows the seasonal cycle of the shortwave and longwave CRF and the seasonal evolution of the CWP over the AMR (20°–50°N, 70°–130°E). The model captures the seasonal evolution of the shortwave CRF and longwave CRF and the CWP reasonably well. For example, the anomalies in the shortwave CRF gradually increase from −13 W m^{-2} in winter (December–January–February) to 40 W m^{-2} in summer

(June–July–August). FAMIL1.1 shows similar characteristics, with the anomalies varying from −16 W m^{-2} to 45 W m^{-2}. This means that the model gives an equivalent magnitude of shortwave CRF to the observations. However, the anomalies in the CWP vary from nearly −45 W m^{-2} in winter to 100 W m^{-2} in summer in the observational dataset, but from −90 W m^{-2} to 135 W m^{-2} in the FAMIL1.1, which means that the model shows a much stronger variability for the CWP.

Except for the seasonal cycle, previous studies have also shown that there are seasonal differences between summer and winter for the CRF over the AMR (Chen and Liu, 2005; Li et al., 2017a). To further evaluate the model's performance in reproducing this feature, the geographic distribution of the CRF from FAMIL1.1 was compared with observations over the AMR during summer and winter time (Fig. 8 and Fig. 9). Observationally, the main feature of the CRF in summer is that there are larger shortwave CRF over the AMR, especially
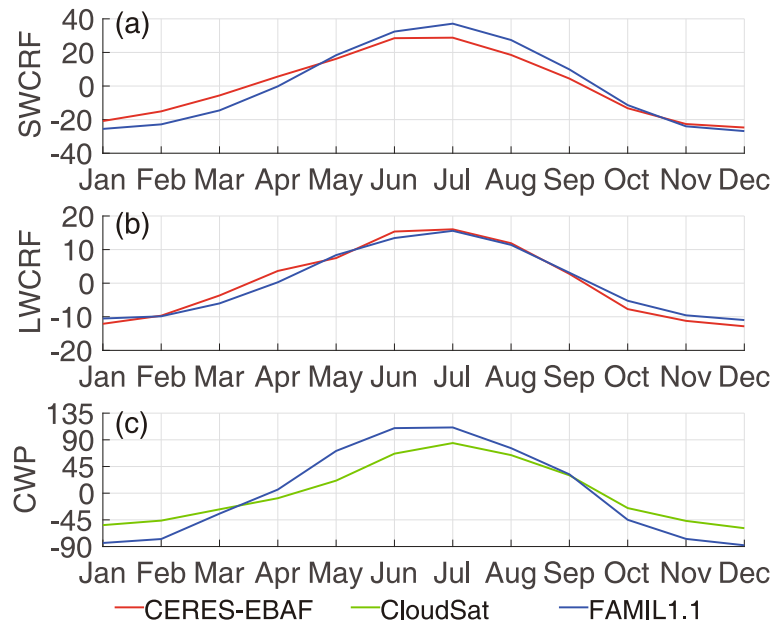
Fig. 7. Seasonal cycle of cloud radiation forcing (units: W m^{-2}) and cloud water path (units: mg m^{-2}) from FAMIL1.1 and observation (CERES-EBAF/CloudSat) in the AMR (20°–50°N, 70°–130°E): (a) shortwave cloud radiation forcing (SWCRF); (b) longwave cloud radiation forcing (LWCRF); (c) cloud water path (CWP). Axes intervals have been subtracted from their annual mean values.
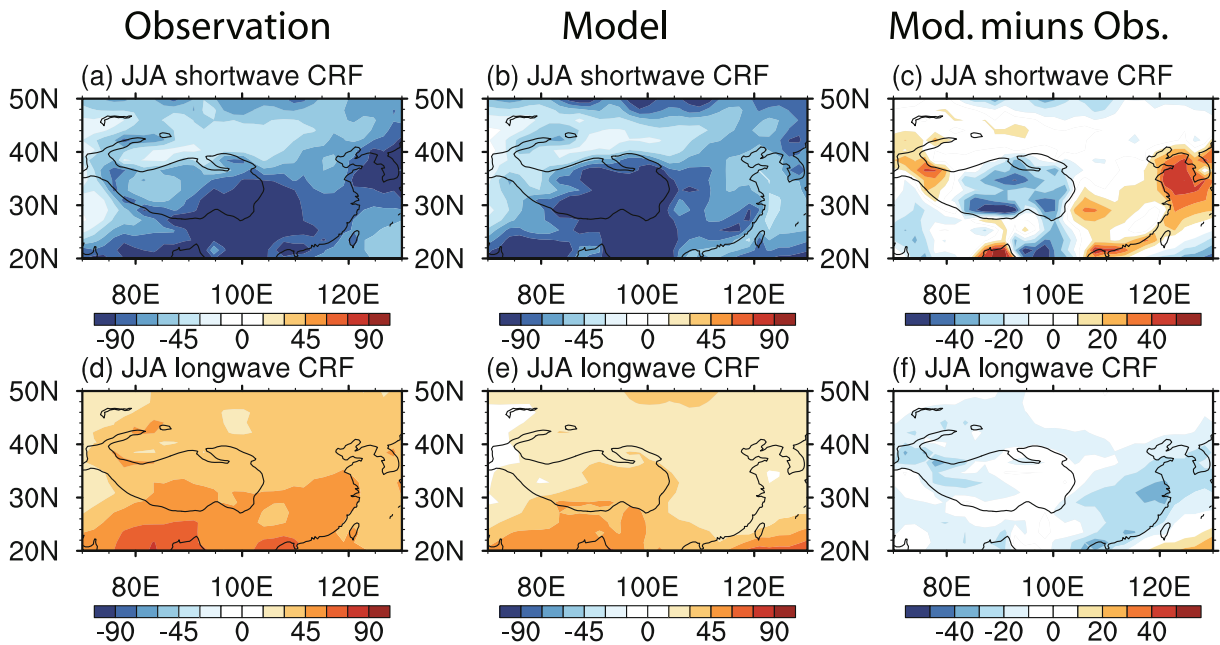

Fig. 8. Geographic distribution of cloud radiation forcing from FAMIL1.1 and observation (CERES-EBAF) over the AMR (20°–50°N, 70°–130°E) in summer (June–July–August): (a–c) shortwave cloud radiation forcing; (d–f) longwave cloud radiation forcing. Units: W m^{-2}.

over the southeastern Tibetan Plateau, eastern China, and the East China Sea (Fig. 8a). The average shortwave CRF over the AMR is −69 W m^{-2}. The longwave CRF is larger over the Bay of Bengal and eastern China (Fig. 8d), with a regional mean about 40 W m^{-2} over the whole AMR. FAMIL1.1 reproduces the geographical distribution of the shortwave CRF and longwave CRF in summer well, with an averaged shortwave CRF about −71 W m^{-2} and an averaged longwave CRF about 28 W m^{-2}. However, FAMIL1.1 shows a stronger shortwave CRF over the Tibetan Plateau, but weaker over
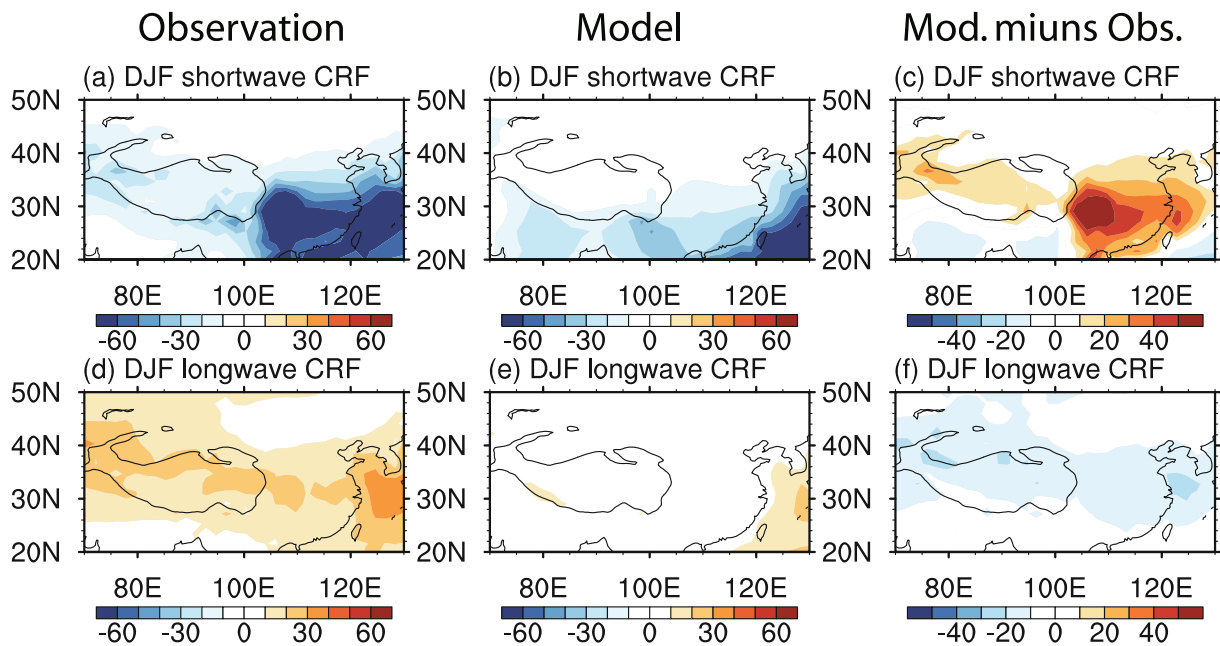
Fig. 9. Geographic distribution of cloud radiation forcing from FAMIL1.1 and observation (CERES-EBAF) over the AMR (20°–50°N, 70°–130°E) in winter (December–January–February): (a–c) shortwave cloud radiation forcing; (d–f) longwave cloud radiation forcing. Units: W m^{-2}.

eastern China and the East China Sea. FAMIL1.1 also underestimates the longwave CRF over the whole AMR. The average negative deviation is about 12 W m^{-2} (or 30%). Figure 9a and 9d also show that the shortwave CRF and longwave CRF decreased greatly over the whole AMR from summer to winter. The averaged shortwave CRF and longwave CRF over the AMR are about −24 and 16 W m^{-2}, respectively. In observation, there is a larger shortwave CRF over eastern China and the East China Sea (> 60 W m^{-2}), but a weaker shortwave CRF over the Tibetan Plateau and its surrounding areas (< 30 W m^{-2}). FAMIL1.1 reproduces the summer–winter contrast for both the shortwave CRF and longwave CRF, but their magnitudes are biased. The averaged shortwave CRF and the longwave CRF over the AMR are about −14 and 5 W m^{-2}, respectively, which means that the average biases are 10 W m^{-2} (40%) and 11 W m^{-2} (66%) over the AMR, respectively. By contrast, FAMIL1.1 seems to underestimate the shortwave CRF over eastern China and the Tibetan Plateau and shows a weaker longwave CRF over the whole AMR.

In theory, the cloud water mass concentration and the cloud droplet radius will both change the shortwave CRF. Smaller cloud droplets usually lead to clouds with a higher albedo (Peng et al., 2002) and thus the reflection of more solar radiation. Figure 10 shows the scatter plots of the seasonal mean shortwave CRF versus the CWP over continental East Asia (20°–40°N, 100°–120°E) and the northern Pacific Ocean (20°–40°N, 170°E–170°W). Comparison of these two areas (land and ocean) highlights the importance of the droplet radius in shortwave CRF. And aerosol conditions difference may be one of the reasons for the land-sea difference

because of its vital importance on the cloud activation process, which can be physically described by CLR2 scheme. Observationally, the slope of these plots over land is larger than over the ocean (slope of 0.29 versus 0.1). One of the possible reasons for the slope difference may be attributed to the difference of the aerosol background over land and ocean area. The land is often much polluted than the ocean, which provides a high concentration of CCNs. As the amount of cloud water increases, more abundant and smaller droplets are produced over the land than over the ocean, resulting in a stronger CRF (greater slope). This relationship can also be reproduced in FAMIL1.1, but the differences between the ocean and land are less significant (slope of 0.21 versus 0.08) than observed. The reason may be that aerosol mass concentration over East Asian used in this study is largely underestimated than observed (Li et al., 2014a), while comparable over oceans to some degree in FAMIL1.1. This is also seen in the distribution of the AOD. In general, the model can simulate the contrast between the land and oceans in terms of the association between the cloud water content and shortwave CRF, but this association is weaker over East Asia in FAMIL1.1 than observed.

5.   Discussions and conclusions

This study describes the incorporation of a two-moment (mass and number) cloud microphysics scheme into FAMIL1.1 with the aim to simulate cloud microphysical processes more realistically, including the subgrid-scale updraft velocity for cloud droplet activation. The global and regional characteristics of the energy balance and CRF simulated by
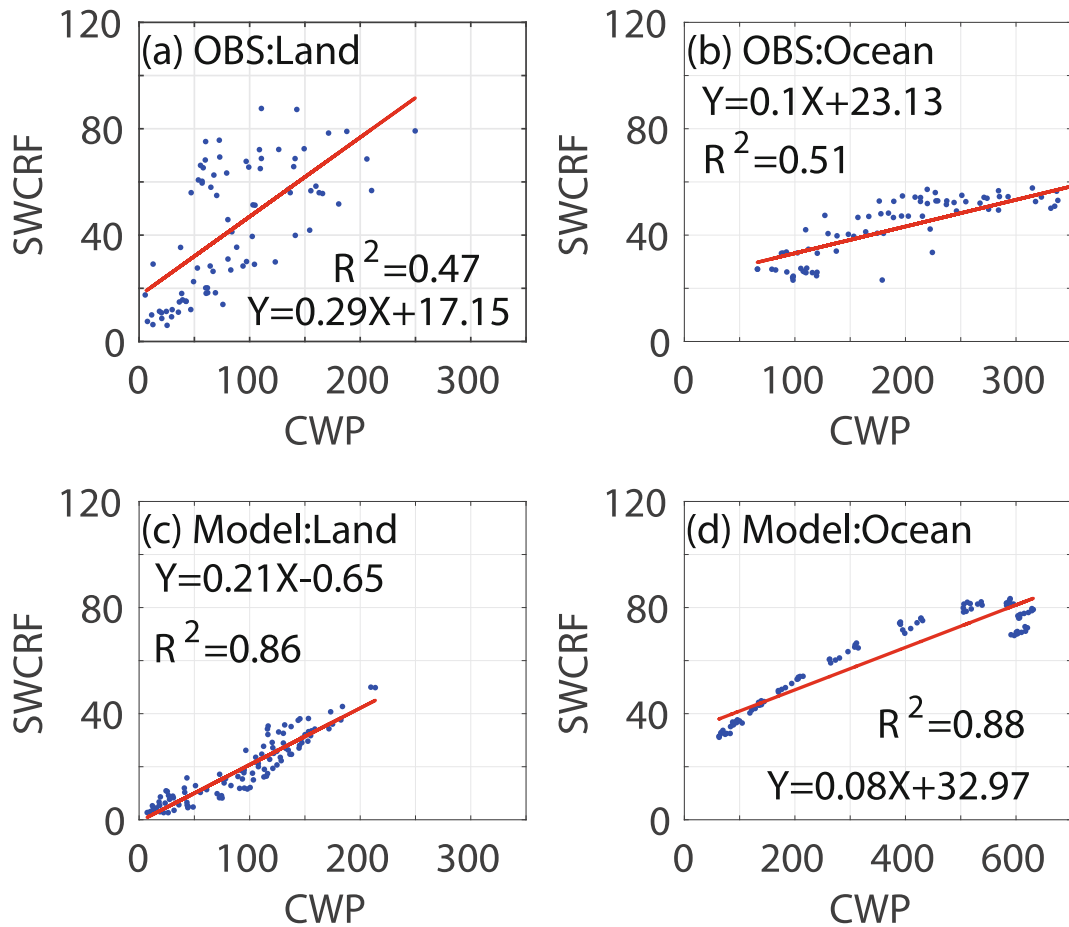
Fig. 10. Scatterplots of the (a, b) observed and (c, d) modeled (FAMIL1.1) seasonal mean shortwave cloud radiation forcing (SWCRF) versus cloud water path (CWP) over (a, c) continental East Asia (20°–40°N, 100°–120°E) and (b, d) the northern Pacific Ocean (20°–40°N, 170°E–170°W).

FAMIL1.1 was evaluated using a comprehensive suite of observational and reanalysis data.

The global annual means of the simulated radiative/heat fluxes in FAMIL1.1, both at the TOA and at the Earth's surface, generally agree well with the observational/reanalysis data. FAMIL1.1 also simulates well in the seasonal cycle and amplitude of the radiation and surface heat fluxes, suggesting that the CLR2 scheme has been successfully introduced into FAMIL1.1.

Also studied was the geographic distribution of the TOA radiative flux and CRF, revealing that FAMIL1.1 reproduces the geographic distribution of the radiation fluxes with a high spatial correlation to observations. The main regional bias is that the net radiative flux over the mainland in FAMIL1.1 is less than that in the observational data, with large negative deviations in northern Africa and northern South America. By contrast, the eastern oceans (marine stratocumulus region) show positive deviations, in good correspondence with the CRF. Further analysis shows that the deviations of the CRF can be partly ascribed to the simulated deviations of the CWP and the amount of high cloud. The model is also able to reproduce the seasonal evolution of the CRF and CWP over East Asia. Furthermore, it reproduces the summer–winter contrast for the geographic distribution of both the longwave CRF and shortwave CRF over the AMR, and simulates the contrast between the land and oceans in terms of the association between the cloud water content and shortwave CRF.

In conclusion, FAMIL1.1 performs well in the simulating of the global energy balance as well as the regional features over the AMR, as verified by investigating its spatial and temporal features. However, there is a large simulation bias in terms of CWP and the amount of high cloud over both the land and ocean, concentrating the simulated deviations in the radiative flux. The reasons for these simulation biases will be investigated in future work based on the large-scale atmospheric circulation, precipitation, and other detailed outputs from the COSP simulator. The present study uses a uniform assumption to derive the vertical velocity in the PBL scheme to determine the change of saturation. The uncertainty in PBL scheme as well as the sub-grid-scale velocity should also be tested in future work. Currently, the aerosol concentration in FAMIL1.1 is prescribed, but work is now taking place on an aerosol module that determines the aerosol concentration dynamically. The impact of the horizontal resolution and air–sea coupling processes on the performance of the model also needs to be studied further.
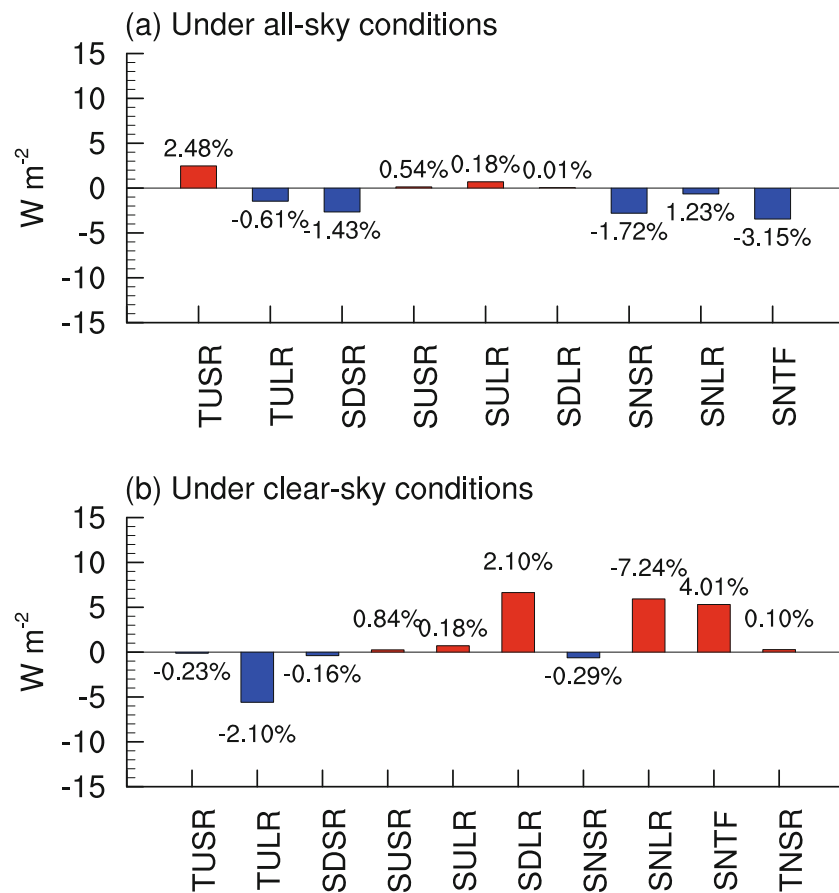
APPENDIX

Fig. A1. Annual global mean energy balance bias (FAMIL1.1 minus CERES-EBAF) at the top of the atmosphere (TOA) and at the Earth's surface under (a) all-sky conditions and (b) clear-sky conditions. Units: W m^{-2}. The relative deviations are listed at the top of each bar. The meaning of the abbreviations is the same as that in Fig. 1., in addition to: SNLR—surface net longwave radiation; SNTF—Surface Net Total Flux; TNSR—TOA Net Shortwave Radiation. This figure is an illustration in parentheses with Table 1 and Table 2.

REFERENCES

Abdul-Razzak, H., and S. J. Ghan, 2000: A parameterization of aerosol activation: 2. Multiple aerosol types. *J. Geophys. Res.*, **105**, 6837–6844, https://doi.org/10.1029/1999JD901161.

Bao, Q., G. X. Wu, Y. M. Liu, J. Yang, Z. Z. Wang, and T. J. Zhou, 2010: An introduction to the coupled model FGOALS1.1-s and its performance in East Asia. *Adv. Atmos. Sci.*, **27**, 1131–1142, https://doi.org/10.1007/s00376-010-9177-1.

Bodas-Salcedo, A., and Coauthors, 2011: COSP: Satellite simulation software for model assessment. *Bull. Amer. Meteor. Soc.*, **92**, 1023–1043, https://doi.org/10.1175/2011BAMS2856.1.

Bony, S., and Coauthors, 2006: How well do we understand and evaluate climate change feedback processes? *J. Climate*, **19**, 3445–3482, https://doi.org/10.1175/JCLI3819.1.

Bretherton, C. S., and S. Park, 2009: A new moist turbulence parameterization in the community atmosphere model. *J. Climate*, **22**, 3422–3448, https://doi.org/10.1175/2008JCLI2556.1.

Chen, B. D., and X. D. Liu, 2005: Seasonal migration of cirrus clouds over the Asian Monsoon regions and the Tibetan Plateau measured from MODIS/Terra. *Geophys. Res. Lett.*, **32**, L01804, https://doi.org/10.1029/2004GL020868.

Chen, G. X., W. C. Wang, and J. P. Chen, 2015: Aerosol-stratocumulus-radiation interactions over the southeast pacific. *J. Atmos. Sci.*, **72**, 2612–2621, https://doi.org/10.1175/JAS-D-14-0319.1.

Chen, G. X., J. Yang, Q. Bao, and W. C. Wang. 2018: Intraseasonal responses of the East Asia summer rainfall to anthropogenic aerosol climate forcing. *Climate Dyn.*, **51**, 3985–3998, https://doi.org/10.1007/s00382-017-3691-0.

Chen, J.-P., and S.-T. Liu, 2004: Physically based two-moment

bulkwater parametrization for warm-cloud microphysics. *Quart. J. Roy. Meteor. Soc.*, **130**, 51–78, https://doi.org/10.1256/qj.03.41.

Cheng, C.-T., W.-C. Wang, and J.-P. Chen, 2007: A modelling study of aerosol impacts on cloud microphysics and radiative properties. *Quart. J. Roy. Meteor. Soc.*, **133**, 283–297, https://doi.org/10.1002/qj.25.

Cheng, C.-T., W.-C. Wang, and J.-P. Chen, 2010: Simulation of the effects of increasing cloud condensation nuclei on mixed-phase clouds and precipitation of a front system. *Atmospheric Research*, **96**, 461–476, https://doi.org/10.1016/j.atmosres.2010.02.005.

Duan, J., and J. T. Mao, 2008: Progress in researches on interaction between aerosol and cloud. *Advances in Earth Science*, **23**, 252–261, https://doi.org/10.11867/j.issn.1001-8166.2008.03.0252. (in Chinese with English abstract)

Ellis, T. D., T. L'Ecuyer, J. M. Haynes, and G. L. Stephens, 2009: How often does it rain over the global oceans? The perspective from CloudSat. *Geophys. Res. Lett.*, **36**, L03815, https://doi.org/10.1029/2008GL036728.

Fan, J. W., Y. Wang, D. Rosenfeld, and X. H. Liu, 2016: Review of aerosol-cloud interactions: Mechanisms, significance, and challenges. *J. Atmos. Sci.*, **73**, 4221–4252, https://doi.org/10.1175/JAS-D-16-0037.1.

Feingold, G., B. Stevens, W. R. Cotton, and R. L. Walko, 1994: An explicit cloud microphysics/LES model designed to simulate the Twomey effect. *Atmospheric Research*, **33**, 207–233, https://doi.org/10.1016/0169-8095(94)90021-3.

Gettelman, A., and S. C. Sherwood, 2016: Processes responsible for cloud feedback. *Current Climate Change Reports*, **2**, 179–189, https://doi.org/10.1007/s40641-016-0052-8.

Harris, L. M., and S. J. Lin, 2014: Global-to-regional nested grid climate simulations in the GFDL high resolution atmospheric model. *J. Climate*, **27**, 4890–4910, https://doi.org/10.1175/JCLI-D-13-00596.1.

Hazra, A., P. Mukhopadhyay, S. Taraphdar, J.-P. Chen, and W. R. Cotton, 2013: Impact of aerosols on tropical cyclones: An investigation using convection-permitting model simulation. *J. Geophys. Res.*, **118**, 7157–7168, https://doi.org/10.1002/jgrd.50546.

Holtslag, A. A. M., and B. A. Boville, 1993: Local versus non-local boundary-layer diffusion in a global climate model. *J. Climate*, **6**, 1825–1842, https://doi.org/10.1175/1520-0442(1993)006<1825:LVNBLD>2.0.CO;2.

Hong, S. Y., J. Dudhia, and S. H. Chen, 2002: A revised approach to ice microphysical processes for the bulk parameterization of clouds and precipitation. *Mon. Wea. Rev.*, **132**, 103–120, https://doi.org/10.1175/1520-0493(2004)132<0103:ARATIM>2.0.CO;2.

Jiang, H. L., G. Feingold, W. R. Cotton, and P. G. Duynkerke, 2001: Large-eddy simulations of entrainment of cloud condensation nuclei into the Arctic boundary layer: May 18, 1998, FIRE/SHEBA case study. *J. Geophys. Res.*, **106**, 15 113–15 122, https://doi.org/10.1029/2000JD900303.

Lamarque, J. F., and Coauthors, 2012: CAM-chem: Description and evaluation of interactive atmospheric chemistry in the Community Earth System Model. *Geoscientific Model Development*, **5**, 369–411, https://doi.org/10.5194/gmd-5-369-2012.

Lee, S. S., and L. J. Donner, 2011: Effects of cloud parameterization on radiation and precipitation: A comparison between single-moment microphysics and double-moment mi-

crophysics. *Terrestrial, Atmospheric and Oceanic Sciences*, **22**, 403–420, https://doi.org/10.3319/TAO.2011.03.03.01.

Li, J. D., W. C. Wang, Z. A. Sun, G. X. Wu, H. Liao, and Y. M. Liu, 2014a: Decadal variation of East Asian radiative forcing due to anthropogenic aerosols during 1850–2100, and the role of atmospheric moisture. *Climate Research*, **61**, 241–257, https://doi.org/10.3354/cr01236.

Li, J. D., J. Y. Mao, and F. Wang, 2017a: Comparative study of five current reanalyses in characterizing total cloud fraction and top-of-the-atmosphere cloud radiative effects over the Asian monsoon region. *International Journal of Climatology*, **37**, 5047–5067, https://doi.org/10.1002/joc.5143.

Li, J.-X., Q. Bao, Y.-M. Liu, and G.-X. Wu, 2017b: Evaluation of the computational performance of the finite-volume atmospheric model of the IAP/LASG (FAMIL) on a high-performance computer. *Atmospheric and Oceanic Science Letters*, **10**, 329–336, https://doi.org/10.1080/16742834.2017.1331111.

Li, L. J., and Coauthors, 2013: The flexible global ocean-atmosphere-land system model, grid-point version 2: FGOALS-g2. *Adv. Atmos. Sci.*, **30**, 543–560, https://doi.org/10.1007/s00376-012-2140-6.

Li, L. J., and Coauthors, 2014b: The flexible global ocean–atmosphere–land system model, grid-point version 2: FGOALS-g2. *Flexible Global Ocean-Atmosphere-Land System Model: A Modeling Tool for the Climate Change Research Community*, T. J. Zhou et al., Eds., Springer, 39–43, https://doi.org/10.1007/978-3-642-41801-3.

Lim, K. S. S., and S. Y. Hong, 2010: Development of an Effective double-moment cloud microphysics scheme with prognostic cloud condensation nuclei (CCN) for weather and climate models. *Mon. Wea. Rev.*, **138**, 1587–1612, https://doi.org/10.1175/2009MWR2968.1.

Lin, Y. L., R. D. Farley, and H. D. Orville, 1983: Bulk parameterization of the snow field in a cloud model. *J. Appl. Meteor.*, **22**, 1065–1092, https://doi.org/10.1175/1520-0450(1983)022<1065:BPOTSF>2.0.CO;2.

Morrison, H., J. A. Curry, and V. I. Khvorostyanov, 2005: A new double-moment microphysics parameterization for application in cloud and climate models. Part I: Description. *J. Atmos. Sci.*, **62**, 1665–1677, https://doi.org/10.1175/JAS3446.1.

Peng, Y. R., U. Lohmann, R. Leaitch, C. Banic, and M. Couture, 2002: The cloud albedo-cloud droplet effective radius relationship for clean and polluted clouds from RACE and FIRE.ACE. *J. Geophys. Res.*, **107**, 4106, https://doi.org/10.1029/2000JD000281.

Pinto, J. O., 1998: Autumnal mixed-phase cloudy boundary layers in the arctic. *J. Atmos. Sci.*, **55**, 2016–2038, https://doi.org/10.1175/1520-0469(1998)055<2016:AMPCBL>2.0.CO;2.

Reisner, J., R. M. Rasmussen, and R. T. Bruintjes, 1998: Explicit forecasting of supercooled liquid water in winter storms using the MM5 mesoscale model. *Quart. J. Roy. Meteor. Soc.*, **124**, 1071–1107, https://doi.org/10.1002/qj.49712454804.

Roh, W., M. Satoh, and T. Nasuno, 2017: Improvement of a cloud microphysics scheme for a global nonhydrostatic model using TRMM and a satellite simulator. *J. Atmos. Sci.*, **74**, 167–184, https://doi.org/10.1175/JAS-D-16-0027.1.

Rosenfeld, D., S. Sherwood, R. Wood, and L. Donner, 2014: Climate effects of aerosol-cloud interactions. *Science*, **343**, 379–380, https://doi.org/10.1126/science.1247490.

Salzmann, M., Y. Ming, J. C. Golaz, P. A. Ginoux, H. Morrison, A. Gettelman, M. Krämer, and L. J. Donner, 2010: Two-

moment bulk stratiform cloud microphysics in the GFDL AM3 GCM: Description, evaluation, and sensitivity tests. *Atmospheric Chemistry and Physics*, **10**, 8037–8064, https://doi.org/10.5194/acp-10-8037-2010.

Sassen, K., and Z. E. Wang, 2008: Classifying clouds around the globe with the CloudSat radar: 1-year of results. *Geophys. Res. Lett.*, **35**, L04805, https://doi.org/10.1029/2007GL032591.

Seifert, A., and K. D. Beheng, 2006: A two-moment cloud microphysics parameterization for mixed-phase clouds. Part 1: Model description. *Meteor. Atmos. Phys.*, **92**, 45–66, https://doi.org/10.1007/s00703-005-0112-4.

Stephens, G. L., and Coauthors, 2012: An update on Earth's energy balance in light of the latest global observations. *Nature Geoscience*, **5**, 691–696, https://doi.org/10.1038/ngeo1580.

Wang, W. C., J. P. Chen, I. S. A. Isaksen, I. C. Tsai, K. Noone, and K. Mcguffie, 2012: Climate-chemistry interaction: Future tropospheric ozone and aerosols. *The Future of the World's Climate*, 2nd ed, A. Henderson-Sellers and K. McGuffie, Eds., Elsevier, 367–399, https://doi.org/10.1016/B978-0-12-386917-3.00013-0.

Wang, W. C., G. X. Chen, and Y. Y. Song, 2017: Modeling aerosol climate effects over monsoon Asia: A collaborative research program. *Adv. Atmos. Sci.*, **34**, 1195–1203, https://doi.org/10.1007/s00376-017-6319-8.

Whitby, K. T., 1978: The physical characteristics of sulfur aerosols. *Atmos. Environ.*, **12**, 135–159, https://doi.org/10.1016/0004-6981(78)90196-8.

Wild, M., D. Folini, C. Schär, N. Loeb, E. G. Dutton, and G. König-Langlo, 2013: The global energy balance from a surface perspective. *Climate Dyn.*, **40**, 3107–3134, https://doi.org/10.1007/s00382-012-1569-8.

Wood, R., P. R. Field, and W. R. Cotton, 2002: Autoconversion rate bias in stratiform boundary layer cloud parameterizations. *Atmospheric Research*, **65**, 109–128, https://doi.org/10.1016/S0169-8095(02)00071-6.

Wu, G. X., H. Liu, Y. C. Zhao, and W. P. Li, 1996: A nine-layer atmospheric general circulation model and its performance. *Adv. Atmos. Sci.*, **13**, 1–18, https://doi.org/10.1007/BF02657024.

Yang, J., W. C. Wang, G. X. Chen, Q. Bao, X. Qi, S. Y. Zhou, 2018: Intraseasonal variation of the black carbon aerosol concentration and its impact on atmospheric circulation over the Southeastern Tibetan Plateau. *J. Geophys. Res.*, **123**, 10 881–10 894, https://doi.org/10.1029/2018JD029013.

Zelinka, M. D., D. A. Randall, M. J. Webb, and S. A. Klein, 2017: Clearing clouds of uncertainty. *Nat. Clim. Change*, **7**, 674–678, https://doi.org/10.1038/nclimate3402.

Zhang, X. Y., Y. Q. Wang, T. Niu, X. C. Zhang, S. L. Gong, Y. M. Zhang, and J. Y. Sun, 2012: Atmospheric aerosol compositions in China: Spatial/temporal variability, chemical signature, regional haze distribution and comparisons with global aerosols. *Atmospheric Chemistry and Physics*, **12**, 779–799, https://doi.org/10.5194/acp-12-779-2012.

Zhou, L. J., Y. M. Liu, Q. Bao, H. Y. Yu, and G. X. Wu, 2012: Computational performance of the high-resolution atmospheric model FAMIL. *Atmospheric and Oceanic Science Letters*, **5**, 355–359, https://doi.org/10.1080/16742834.2012.11447024.

Zhou, L. J., and Coauthors, 2015: Global energy and water balance: Characteristics from Finite-volume Atmospheric Model of the IAP/LASG (FAMIL1). *Journal of Advances in Modeling Earth Systems*, **7**, 1–20, https://doi.org/10.1002/2014MS000349.